Performance Modeling and Analysis of a Doubly Yokeless Permanent Magnet Linear Motor With Improved Thrust Force Quality

QIAN WANG[1], (Member, IEEE), **YINGQI CHEN**[1], **YAN GUO**[2], **JUAN ZHANG**[3], **AND YONG LI**[1]

[1]Electrical Engineering Department, Harbin Institute of Technology, Harbin 150001, China
[2]Huawei Technologies Co., Ltd., Shenzhen 518000, China
[3]Industrial Technology Research Institute of Heilongjiang Province, Harbin 150001, China

Corresponding author: Qian Wang (q.wang@hit.edu.cn)

ABSTRACT Permanent magnet linear motors (PMLM) have gained increased popularities in a wide range of applications. However, they generally suffer from considerably lower force densities. In this paper, a novel doubly yokeless PMLM equipped with quasi-Halbach trapezoidal-shape permanent magnets is presented to both increase the thrust force density and suppress the thrust ripple. Both the stator and the translator are yoke-free, and therefore, the increase of the installation space for the windings is conducive to enhancing the magneto-motive force and the thrust density of the motor. An analytical model is developed to predict the magnetic field distribution and electromagnetic performance of the doubly yokeless PMLM, and finite element computations are undertaken to validate the effectiveness and accuracy of the proposed model. The thrust performance is then optimized against magnet parameters under a specific set of volumetric constraints to the improve the thrust force quality. It is shown that the Halbach ratio and bottom angle of the trapezoidal magnets have significant impacts on the thrust force quality (in terms of both the average thrust and thrust ripple), and optimal values for the two parameters are obtained. The benefits of the doubly yokeless PMLM are highlighted by comparisons with a conventional PMLM with iron yokes.

INDEX TERMS Force ripple, permanent magnet linear motor, quasi-Halbach, thrust force, yokeless.

I. INTRODUCTION

Permanent magnet linear motors (PMLM) are finding their applications quickly in a number of applications [1]–[5]. Compared with their rotary-to-linear counterparts, by eliminating the intermediate transmission, the PMSM are able to offer great advantages in terms of reliability, structural integrity, motional revolution, noise and vibration, et al. During the recent past years, along with the technological developments and performance improvement of linear motion systems, there is an urging demand for high-force-density linear machines [6]–[8]. Most recently, a novel type of linear motors, which have no or reduced iron yokes, named 'yokeless PMLM', are put into focus.

For the yokeless PMLM, by eliminating the iron yokes, the installation space for the windings can be increased without

The associate editor coordinating the review of this manuscript and approving it for publication was Kan Liu.

affecting the magnetic load, which leads to improved thrust force density. In literature, several topologies of yokeless machines, including both the rotary type and linear type, have been investigated. A rotary version with axial-flux configuration is presented in [9] and [10], with yokeless and segmented armature. A novel topology of the yokeless PMLM is reported in [11], and it is shown that the absence of the yoke leads to 7.7% higher efficiency and 5.4% higher force density under the same volumetric and thermal constraints. In [12]–[14], a few topologies of flux-switching PMLM with yokeless translators are investigated. And it is found that the thrust capability of the yokeless design can be considerably increased over that with iron yokes. However, it should be noted that all the yokeless motors above are just singly yokeless. That is to say, only the stator or the rotor/translator is yokeless, while the other part still has the yoke. In order to further enhance the motor performance, it is generally desirable to develop a doubly yokeless PMLM.

In this paper, a novel topology of doubly yokeless PMLM is proposed, and the issues pertinent to the analytical modeling, numerical validation and performance optimization of the motor are investigated. Firstly, the analytical model of the motor is established to predict the electromagnetic performance, including the air-gap flux density, back electromotive force (EMF) and thrust force. Finite element computations are then performed to validate the effectiveness of the analytical formula. Secondly, the PMLM is optimized under a specific set of volumetric constraints for improving the thrust force quality, namely enhancing the average thrust force while reducing the force ripple at the same time. And the thrust force quality of the yokeless PMLM is also compared with that of conventional PMLM with iron yokes. And finally, the conclusions are drawn.

II. TOPOLOGY EVOLUTION: FROM YOKED STRUCTURE TO DOUBLY YOKELESS STRUCTURE

In this section, the topology development from the conventional single-sided PMLM to the novel doubly yokeless PMLM is introduced, and the pros and cons of the doubly yokeless topology are given afterwards.

A. SINGLE-SIDED PMLM & DOUBLE-SIDED PMLM

Nowadays, the commercially available PMLM are generally employing single-sided configurations, such as Siemens ® 1FN3-series, Kollmorgen ® IC-series, Tecnotion ® TBM-series, etc. Benefiting from high resolution, high efficiency and fast dynamic response, they have been applied in a wide range of market sectors. However, quite huge unilateral magnetic forces exist in this kind of motors, and special care must be taken to the mechanical support systems, which somewhat restricts their further developments.

For the double-sided PMLM, by employing symmetric structure, the magnetic forces at both sides can cancel each other. And in this way, the linear motor can be designed in slender manner, without compromising too much on the mechanical strength of the motion systems.

Considering the topology of the magnetic circuits, there are two kinds of double-sided PMLM, i.e. the series type and parallel type, as shown in Fig. 1, where the dash blue lines illustrate the flux distribution.

B. PMLM WITH YOKELESS PRIMARY

However, for both the single-sided and double-sided PMLM, they generally suffer from lower force densities. How to reduce the volume or mass while not affecting the output force is a big concern. Focusing on Fig. 1(a), since the flux lines in the primary yoke is with opposite directions for the two sides, the yoke of the armature core can be eliminated, allowing more space available for the windings, which leads to improved force density.

C. PROPOSAL OF DOUBLY YOKELESS PMLM

In order to further enhance the force density, by introducing Halbach-magnetization PM array in the secondary part, the yokes for the PM assembly can also be canceled, leading to a novel doubly yokeless PMLM, and its schematic structure is illustrated in Fig. 2.

D. ADVANTAGES OF DOUBLY YOKELESS PMLM

The proposed doubly yokeless PMLM employs fractional-slot concentrated windings, and coils can be wound on all the teeth or on alternate teeth. The armature core is composed only of teeth, and the lack of yokes allows more space arranged for the windings and permanent magnets under given volumetric constraints, and they are conducive to increased armature MMF and air-gap flux density, and in this way, improved thrust density can be achieved.

For the PM assembly, trapezoidal PM are arranged in two columns symmetrized to the axis of the armature core, and each column is magnetized in quasi-Halbach array to increase the air-gap flux density, to reduce force ripple and to remove the back iron. The function of the horizontal magnetization is acting as a compensating magnetic circuit to increase the air gap flux density under the dominance of the vertical magnetization.

For the motor shown in Fig. 2, the active part of the motor includes 14 poles and 12 slots. If a moving armature core is
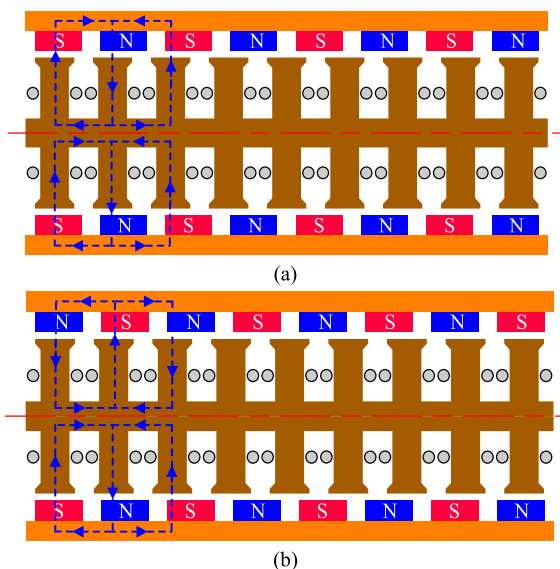

FIGURE 1. Structures of double-sided PMLM. (a) The series type. (b) The parallel type.
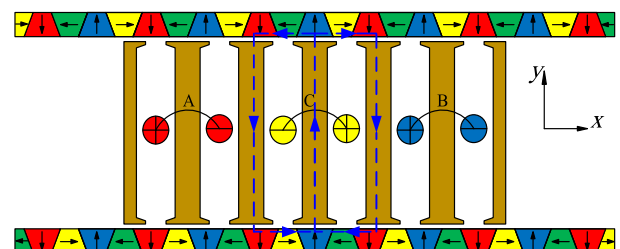

FIGURE 2. Schematic of the novel doubly yokeless PMLM.

adopted, the lack of yokes can decrease the mass of the mover, and hence fast dynamic response can also be achieved.

It should be noted that since all the conductive teeth are separated into single pieces, special care must be taken to the mechanical support systems, and the mechanical strength is somewhat lower than the conventional yoked PMLM.

III. ANALYTICAL MODELING OF MAGNETIC FIELD, EMF, AND THRUST FORCE

In order to facilitate the performance prediction and design optimization of the doubly yokeless PMLM, analytical modeling of the magnetic field is essential. Although the general framework has been well established in literature for analysis and design of the PMLM with regular rectangular-shape permanent magnets either in vertical-array, horizontal-array, quasi-Halbach, or Halbach configurations [15]–[17], there are quite few references on the analytical models for motors with trapezoidal-shape magnets. In [18] and [19], semi-analytical models have been reported for the PMLM with trapezoidal-shape magnets. However, they are just applicable for tubular version instead of the flat PMLM. And further, the models in [18] and [19] are equipped with iron yokes to complete the magnet flux loop. When the iron yokes are eliminated (as shown in Fig. 2), there would be no confinements for the flux linkage on the y-axis directions, and the case would be quite different. Therefore, it is necessary to develop a new analytical model that is suitable for the doubly yokeless PMLM.
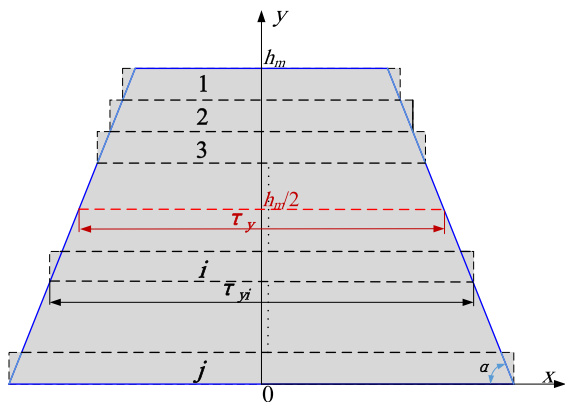

FIGURE 3. Substitution of a trapezoidal magnet with J-layer rectangular magnets.

In the doubly yokeless motor, as the magnets are trapezoidal, Poisson equations in magnet regions become quite complex. Compared with trapezoidal PM, the analytical model of rectangular PM is easier to build. Considering the fact that trapezoidal magnets can be equivalent to the superposition of a number of rectangular magnets (as shown in Fig. 3) without introducing any significant errors due to magnetic saturation, a new method based on superposition principle is proposed. And in this way, the magnetic field and electromagnetic performance of the yokeless linear motor

at both no-load and load conditions can be analytically predicted.

In this section, the analytical model of a linear motor with rectangular-shape quasi-Halbach magnet array is first established, and then the magnetic field generated by trapezoidal PM is derived using superposition method. Due to symmetry, only the magnetic field produced by one-side PM is considered. Further, in order to simplify the analysis, the magnetic circuit is considered to be linear, and the following assumptions are made:

1) The stator and translator are infinitely extended in the x-axis direction, and hence, end-effects can be neglected.

2) The permeability of core is infinite, and the cogging effect is not considered for the time being.

3) The permanent magnets are magnetized uniformly in the magnetization direction, and the relative permeability of the PM is 1.
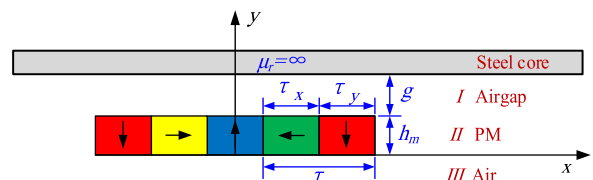

FIGURE 4. Model of the yokeless PMLM considering different magnetic field regions.

Accordingly, for the linear motor equipped with rectangular magnets, the model can be divided into three magnetic field regions, as shown in Fig. 4, where g is the air-gap thickness, h_m is the magnet thickness, τ is the pole pitch, and τ_x and τ_y refer to the magnet width magnetized in horizontal and vertical directions, respectively.

The magnetic field in each region can be calculated by magnetic vector potential, and the governing equations are

$$\nabla^2 A_{I,III} = 0 \quad \text{in Region} \quad I \text{ and } III \quad (1)$$
$$\nabla^2 A_{II} = -\mu_0 \nabla \times M \quad \text{in Region } II \quad (2)$$

where μ_0 is the permeability of air, M is the PM remanent magnetization, and it is related to the magnet remanence B_r by $M = B_r/\mu_0$. B_r is the residual flux density of the magnets.

Boundary conditions in the three regions are given by

$$\begin{cases} H_{xI}|_{y=g+h_m} = 0 \\ H_{xII}|_{y=h_m} = H_{xI}|_{y=h_m} \\ B_{yII}|_{y=h_m} = B_{yI}|_{y=h_m} \\ B_{yII}|_{y=0} = B_{yIII}|_{y=0} \\ H_{xII}|_{y=0} = H_{xIII}|_{y=0} \\ B_{yIII}|_{y=-\infty} = 0 \end{cases} \quad (3)$$

And H_{xII} is related to M and B_{xII}, with the expression given by

$$H_{xII} = \frac{B_{xII}}{\mu_r\mu_0} - \frac{\mu_0 M_x}{\mu_r\mu_0} \quad (4)$$

It should be noted that since there is no yoke for the PM in the motor, the boundary condition at Region *III* is different from that in conventional PMLM with iron yokes.

By solving these equations, the magnetic flux density in the air-gap region can be derived, with the expressions as

$$
\begin{cases}
B_{xI}(x,y) = \sum_{n=1}^{\infty} m_n(A_{n1}e^{m_ny} - B_{n1}e^{-m_ny})sin(m_nx) \\
B_{yI}(x,y) = -\sum_{n=1}^{\infty} m_n(A_{n1}e^{m_ny} + B_{n1}e^{-m_ny})cos(m_nx)
\end{cases}
\tag{5}
$$

where $m_n = (2n-1)\pi/\tau$, and the coefficients A_{n1} and B_{n1} are derived from boundary conditions and are given in Appendix A.

For the linear motor with trapezoidal magnets, the magnetic field can be obtained by superimposing the magnetic field generated by each layer of rectangular magnets if magnetic saturation is not taken into account. Before this, the dimension relationship between the trapezoidal magnet and rectangular magnet should be established.

For the magnet magnetized in vertical direction in the down layer, the width of the ith-layer rectangular magnet (as shown in Fig. 3) is given by

$$
\tau_{yi} = \tau_y - \frac{h_m}{tan(\alpha)} + \frac{2h_m(i-1)}{(j-1)tan(\alpha)}
\tag{6}
$$

where h_m is the height of the magnets and α is the bottom angle of magnets. And accordingly, for the magnet magnetized in horizontal direction in the down layer, the width of the ith-layer rectangular magnet is given by

$$
\tau_{xi} = \tau - \tau_{yi}
\tag{7}
$$

As a result, the air-gap flux density generated by trapezoidal magnets can be obtained by adding those generated by *j*-layer rectangular magnets together, and the expressions are as (8), as shown at the bottom of this page, where $A_{i,n1}$ and $B_{i,n1}$ are given in Appendix B.

The model established above can only be applied to slotless motors. By utilizing the relative permeance, the model can be extended to account for slotting effects. The relative permeance function of the slotted air-gap region is given by [16]

$$
\lambda'(x,y) = a_0 + \sum_{n=1}^{\infty} a_n cos\left[\frac{2\pi}{\tau_s}n(x + b_{sa})\right]
\tag{9}
$$

where τ_s is the slot pitch, b_{sa} is the relative distance between axes of phase windings and base position, and the coefficients a_0 and a_n are given in Appendix C.

TABLE 1. Main parameters of the doubly yokeless PMLM.

| Parameters	Symbol (Unit)	Value
Pole-slot combination	/	14-pole/12-slot
Depth in *z*-axis direction	L_a (mm)	52
PM height	h_m (mm)	5
Width of PM magnetized in *y*-axis direction	τ_y (mm)	6
Width of PM magnetized in *x*-axis direction	τ_x (mm)	6
Pole pitch	τ (mm)	12
Bottom angle of PM magnetized in *y*-axis direction	α (°)	120
Air-gap length	g (mm)	1.0
Slot width	b_s (mm)	4.5
Remanent flux density of PM	B_r (T)	1.2
Number of turns in series per phase	N_s	1008
Mover velocity	v_s (m/s)	1.0
RMS value of phase current	I_{rms} (A)	1.0
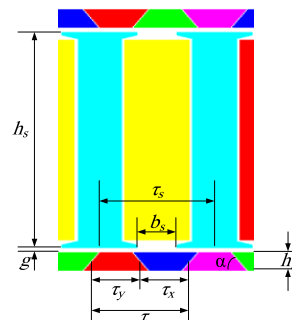
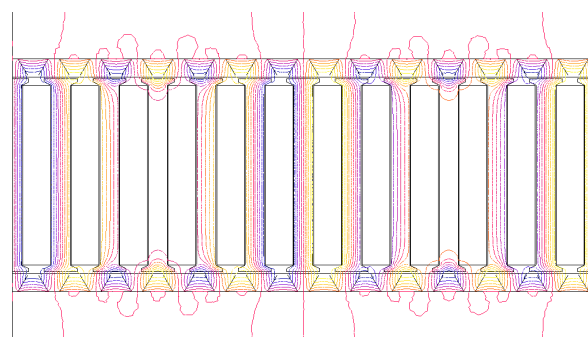**FIGURE 5. Illustration of main geometric parameters.**

FIGURE 6. Open-circuit magnetic flux distribution.

Hence, the magnetic field distribution considering the effects of slot openings is derived from the product of the field neglecting slot openings and the relative permeance function,

$$
\begin{cases}
B_{x\_tra}(x,y) = \sum_{i=1}^{j}\sum_{n=1}^{\infty} m_n \left(A_{i,n1}e^{m_n\left(y + \frac{ih_m}{j} - h_m\right)} - B_{i,n1}e^{-m_n(y + \frac{ih_m}{j} - h_m)}\right) sin(m_nx) \\
B_{y\_tra}(x,y) = -\sum_{i=1}^{j}\sum_{n=1}^{\infty} m_n(A_{i,n1}e^{m_n\left(y + \frac{ih_m}{j} - h_m\right)} + B_{i,n1}e^{-m_n(y + \frac{ih_m}{j} - h_m)})cos(m_nx)
\end{cases}
\tag{8}
$$

i.e.,

$$B_{yslot}(x, y) = B_{y\_tra} \cdot \lambda'(x, y) \quad (10)$$

Taking phase winding A as an example, when the axis of the magnet magnetized in the y-positive direction coincides with the axis of the A-phase, it is used as the starting point for calculating the flux linkage in phase winding A. The flux linkage of phase winding A is expressed as follows

$$\psi_a = \sum_{i=1}^{j} \sum_{n=1}^{\infty} \phi_{pi,n} cos(m_n x) \quad (11)$$

where

$$\phi_{pi,n} = 2\alpha N_s N_c L_a K_{ri,n} K_{dn} K_{pn} \quad (12)$$

in which

$$K_{ri,n} = A_{i,n1} e^{m_n(g+i\frac{hm}{j})} + B_{i,n1} e^{-m_n(g+i\frac{hm}{j})} \quad (13)$$

$$K_{pn} = sin(m_n.\frac{\tau_s}{2}) \quad (14)$$

where N_s is the number of turns in series per phase, N_c is the turn number connected in series per phase, L_a is the depth of

armature core in z-axis direction, and K_{dn} is the distribution factor. The back EMF of phase winding A is given by

$$e_a = -\frac{d\psi_a}{dt} = \sum_{i=1}^{j} \sum_{n=1}^{\infty} K_{Ei,n} \cdot v_s \cdot \sin(m_n x) \quad (15)$$

$$K_{Ei,n} = 2m_n\beta N_s N_c L_a K_{ri,n} K_{dn} K_{pn} \quad (16)$$

where β refers to the average value of the relative permeance function of air gap, and here it is used to calculate the air-gap flux density reduced by slotting, and v_s is the mover velocity.

When the three phase windings are excited by sinusoidal currents corresponding to its phase, the electromagnetic thrust is given by

$$
\begin{aligned}
F &= \frac{e_a \cdot i_a + e_b \cdot i_b + e_c \cdot i_c}{v_s} \\
&= -\sqrt{2}I_{rms} \sum_{i=1}^{j} \sum_{n=1}^{\infty} K_{Ei,n} \Bigg[sin(m_n x) sin(\omega t) \\
&\quad + sin\left(m_n x - \frac{2\tau}{3}\right) sin\left(\omega t - \frac{2\pi}{3}\right) \\
&\quad + sin\left(m_n x + \frac{2\tau}{3}\right) sin\left(\omega t + \frac{2\pi}{3}\right) \Bigg]
\end{aligned} \quad (17)
$$

where I_{rms} is the effective value of the phase current.

IV. NUMERICAL VALIDATIONS

In this section, the results obtained by the analytical model are compared with finite element analysis (FEA) to verify the
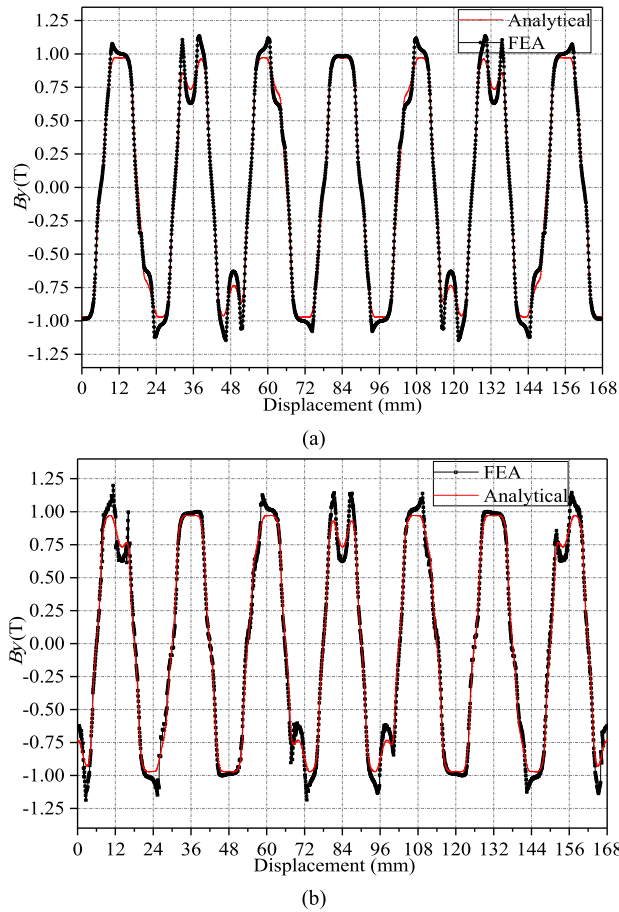
FIGURE 7. Waveforms of air-gap flux density at different positons. (a) The y-axis magnetized PM aligned with tooth center. (b) The y-axis magnetized PM aligned with slot center.
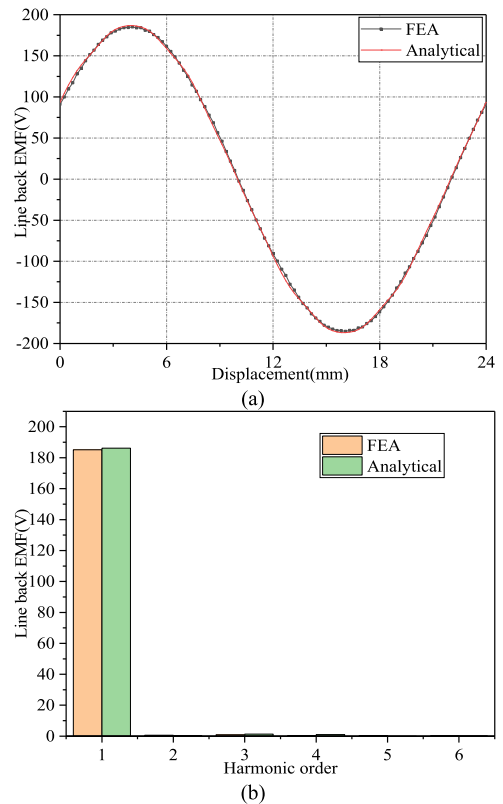
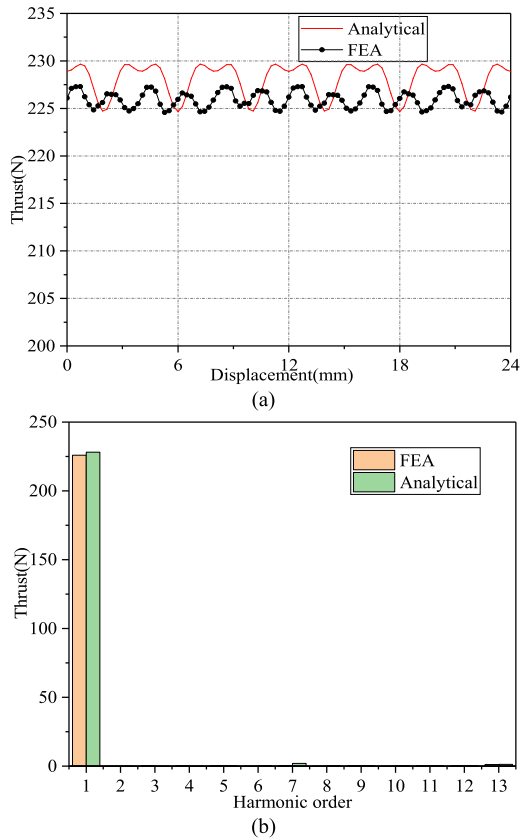**FIGURE 8.** Comparison of Line Back EMF. (a) Waveforms. (b) FFT results.

FIGURE 9. Comparison of thrust force. (a) Waveforms. (b) FFT results.

FIGURE 10. Variation of thrust with τy and α. (a) Average thrust force. (b) Thrust ripple.

validity. Fig. 5 illustrates the main parameters of the doubly yokeless PMLM, with their values listed in Table 1.

The FE solutions were obtained by applying a periodic boundary condition at $x = \pm 7\tau_p$ to exclude the end effect, and imposing Dirichlet boundary conditions at other bounding surfaces.

Fig. 6 shows the FE-predicted magnetic field distribution in open-circuit condition within an active length of 14 poles. It would be of interest to note that there are still a few of flux lines going out of the motor. In conventional PMLM with yokes, since the yokes are generally made of irons with high magnetic permeability, the flux would be confined with the geometric limits composed of iron-yokes. However, in the novel doubly yokeless PMLM, the flux cannot be confine to a limited region any more, due to the absence of yokes for the magnets. One may wonder if the quasi-Halbach configuration could restrain the flux go out. Although the ideally-Halbach magnet array could completely cancel the flux in the yokes, the quasi-Halbach array fails, since it is just a simpler form.

Fig. 7 shows the air-gap flux density waveforms when the magnet magnetized in y-axis positive direction aligns with the tooth center line and the slot center line, respectively.

It can be seen that the air-gap flux density waveforms obtained by analytical and numerical methods basically show good agreement in most areas. The error main lies in the regions near slot openings, where the FEA results are slightly larger than those by analytical method. The reason for this
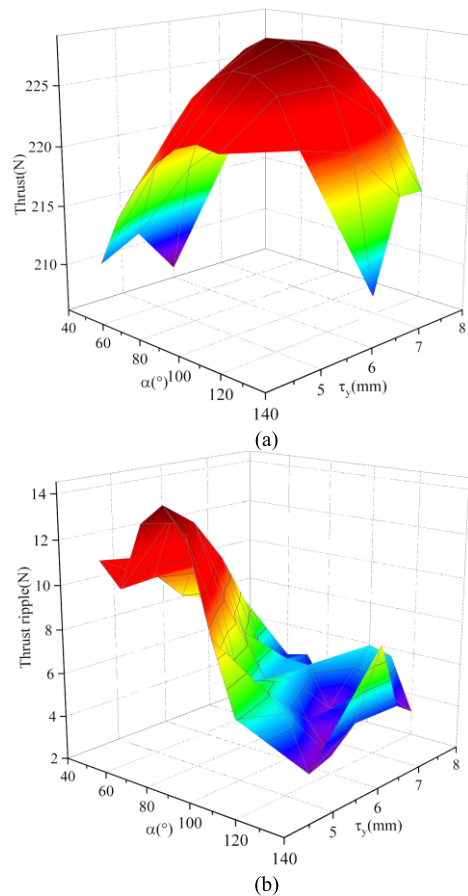
phenomenon is that when the y-axis magnetized magnets and the teeth are staggered, the magnetic flux gathers at the teeth, which in turn increase the flux density nearby. However, the analytical model cannot take this so-called 'corner effect' into account.

Fig. 8 compares the back-EMF waveforms obtained by analytical method and FEA. As will be seen, the back-EMF waveforms are in good agreement.

Fig. 9 shows the comparison of the thrust forces with three phases fed with symmetric currents. It can be observed that the analytically-predicted thrust force is slightly larger than FE-predicted value. It is due mainly to the effect of magnetic saturation, which is not accounted for in the analytical model, since increased electrical loading causes more saturation, which in turn is responsible for lower force. Anyway, they are quite close.

V. IMPROVEMENT OF THRUST FORCE QUALITY
The shape and key parameters of trapezoidal permanent magnets have significant effects on air-gap flux density of the motor, which in turn affects the thrust force quality, i.e., the average thrust force and thrust ripple. In this section, the pole pitch τ is fixed at 12mm, and τ_y and α are parameterized to investigate their effects on the thrust force.
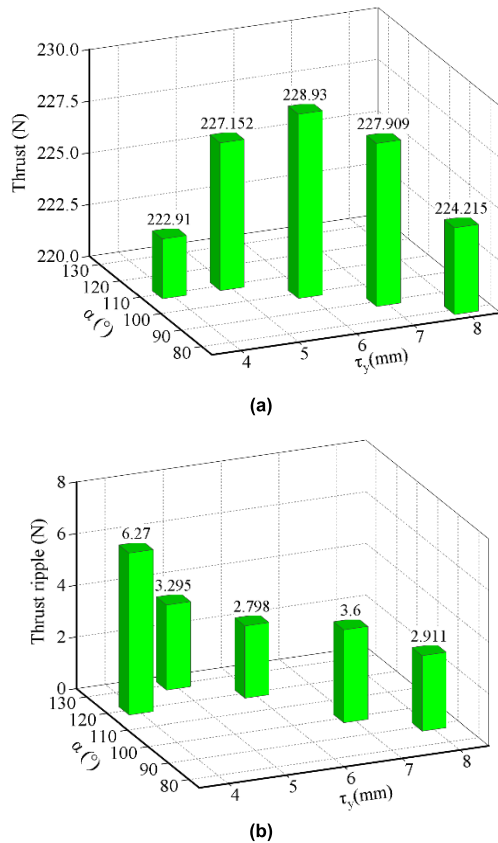
(a)

(b)

FIGURE 11. Optimal values of α for maximum thrust and minimum ripple with different τ_y. (a) Maximum thrust values vs. τ_y and α. (b) Minimum thrust ripple values vs. τ_y and α.

Fig. 10 shows the influences of τ_y and α on the average thrust force and thrust ripple when three phases are fed with rated symmetrical currents.

For Fig. 10(a), it can be seen that when τ_y or α is too large or too small, the self-shielding effect of the PM arranged in quasi-Halbach becomes worse, which leads to a significant decrease the average thrust force. While for the thrust ripple in Fig. 10(b), their relationships are relatively complex.

More specifically, by sweep τ_y from 4mm to 8mm with an incremental step of 1mm, the optimal values of α for maximum thrust and minimum ripple are shown in Fig. 11(a) and Fig. 11(b), respectively. And the corresponding force values are also shown. As will be seen, the maximum thrust force of 228.93N can be achieved when τ_y = 6mm and α = 100° (with the thrust ripple of 5.947N), while the case for minimum ripple is 2.798N when τ_y = 6mm and α = 120°(with the average thrust of 225.951).

VI. COMPARISON OF THRUST FORCE QUALITY WITH YOKED PMLM

In this section, the thrust force of the doubly yokeless PMLM is compared with that of a conventional double-sided PMLM with iron yokes (as illustrated in Fig.1) with the same volumes.

Table 2 compares the main parameters and performance of the two motors. The yokeless motor has been optimized for

TABLE 2. Comparison between yokeless and yoked PMLM.

Dimension / Parameter	Unit	Yokeless	Yoked
Height (in *y*-axis direction)	mm	78	78
Length (in *x*-axis direction)	mm	168	168
Depth (in *z*-axis direction)	mm	52	52
PM height	mm	5	5
τ_y	mm	6	6
α	°	120	90
I_{rms}	A	1	1
Average thrust force	N	225.951	159.971
Thrust ripple	N	2.798	6.254

minimum thrust ripple. It can be seen that the novel doubly yokeless topology leads to 41.2% higher thrust force and 55.3% lower thrust ripple than the traditional PMLM. It is also of interest to note that the absence of yoke in armature core reduces the mass of the mover, which is conducive to achieving better dynamic performance.

VII. CONCLUSION

This paper has addressed analytical modeling and performance improvement of a novel doubly yokeless PMLM equipped with quasi-Halbach trapezoidal-shape magnets. And the following conclusions have been drawn:

(1) By splitting a trapezoidal permanent magnet into a number of rectangular permanent magnets, the electromagnetic performance of the doubly yokeless PMLM has been analytically derived, and the effectiveness is validated by finite element computations. The work serves as a valuable tool for precise and fast optimization design of the yokeless PMLM.

(2) The magnet parameters, especially the Halbach ratio and bottom angle of the trapezoidal magnets, have significant impacts on the thrust force quality, in terms of both the average thrust force and the thrust ripple.

(3) Compared with conventional double-sided PMLM with iron yokes, the proposed doubly yokeless PMLM leads to 41.2% higher thrust force and 55.3% lower thrust ripple in the case study.

APPENDIX A
Definition of A_{n1}, B_{n1}

$$A_{n1} = \frac{2\tau B_r}{(2n-1)^2 \pi^2} \left[\cos\left(\frac{\tau_y m_n}{2}\right) + \sin\left(\frac{\tau_y m_n}{2}\right) \right]$$
$$\cdot e^{-m_n(2g+h_m)} \left(e^{-m_n h_m} - 1 \right),$$

$$B_{n1} = \frac{2\tau B_r}{(2n-1)^2 \pi^2} \left[\cos\left(\frac{\tau_y m_n}{2}\right) + \sin\left(\frac{\tau_y m_n}{2}\right) \right]$$
$$\cdot e^{-m_n h_m} \left(e^{-m_n h_m} - 1 \right)$$

APPENDIX B
Definition of A_{n1}, B_{n1}

$$A_{i,n1} = \frac{2\tau B_r}{(2n-1)^2 \pi^2}\left[cos\left(\frac{\tau_{yi}m_n}{2}\right) + sin\left(\frac{\tau_{yi}m_n}{2}\right)\right]$$
$$\cdot e^{-2m_n\left(g+\frac{ih_m}{j}\right)}\left(1 - e^{-\frac{m_n h_m}{j+1}}\right),$$

$$B_{i,n1} = \frac{2\tau B_r}{(2n-1)^2 \pi^2}\left[cos\left(\frac{\tau_{yi}m_n}{2}\right) + sin\left(\frac{\tau_{yi}m_n}{2}\right)\right]$$
$$\cdot \left(1 - e^{-\frac{m_n h_m}{j+1}}\right)$$

APPENDIX C
Definition of a_0 and a_n

$$a_0 = \frac{1}{K_c}\left[1 - 1.6\frac{b_s}{\tau_s}\beta(y)\right]$$

$$a_n = -\frac{4}{n\pi}\beta(y)\left[0.5 + \frac{(nb_s/\tau_s)^2}{0.78125 - 2(nb_s/\tau_s)^2}\right]sin\left(1.6n\pi\frac{b_s}{\tau_s}\right)$$

$$\beta(y) = \frac{B_{max} - B_{min}}{2B_{max}} = \frac{1}{2} - \frac{1}{2\sqrt{1 + \left(\frac{\tau_s}{2g'}\right)^2(1+v^2)}}$$

v is determined by

$$y\frac{\pi}{b_s} = \frac{1}{2}ln\left(\frac{\sqrt{\alpha^2+v^2}+v}{\sqrt{\alpha^2+v^2}-v}\right) + \frac{2g'}{b_s}arctan\left(\frac{2g'}{b_s}\frac{v}{\sqrt{\alpha^2+v^2}}\right).$$

where τ_s is the slot pitch, b_s is the slot width. And the Carter coefficient K_c is given by

$$K_c = \left[1 - \frac{2b_s}{\tau_s\pi}arctan\left(\frac{b_s}{2g'}\right) + \frac{4g'}{\tau_s\pi}ln\left(\sqrt{1 + \left(\frac{\tau_s}{2g'}\right)^2}\right)\right]^{-1}$$

where $g' = g + h_m/\mu_r$, and it refers to the effective length of the air gap.

REFERENCES

[1] H. Gurol, "General atomics linear motor applications: Moving towards deployment," *Proc. IEEE*, vol. 97, no. 11, pp. 1864–1871, Nov. 2009.
[2] R. W. Cao, Y. Jin, M. H. Lu, and Z. Zhang, "Quantitative comparison of linear flux-switching permanent magnet motor with linear induction motor for electromagnetic launch system," *IEEE Trans. Ind. Electron.*, vol. 65, no. 9, pp. 51011–51020, Sep. 2018.
[3] Q. Wang, J. Wang, B. Zhao, Y. Li, H. Zhao, and J. Ma, "Modeling, design optimization, and verifications of permanent magnet linear actuators for structural vibration mitigation applications," *IEEE Trans. Magn.*, vol. 53, no. 11, Nov. 2017, Art. no. 8205304.
[4] J. Wang, W. Wang, and K. Atallah, "A linear permanent-magnet motor for active vehicle suspension," *IEEE Trans. Veh. Technol.*, vol. 60, no. 1, pp. 55–63, Jan. 2011.
[5] J. Wang, Z. Lin, and D. Howe, "Analysis of a short-stroke, single-phase, quasi-Halbach magnetised tubular permanent magnet motor for linear compressor applications," *IET Electr. Power Appl.*, vol. 2, no. 3, pp. 193–200, May 2008.
[6] Z. Liu, W. Zhao, J. Ji, and Q. Chen, "A novel double-stator tubular vernier permanent-magnet motor with high thrust density and low cogging force," *IEEE Trans. Magn.*, vol. 51, no. 7, Jul. 2015, Art. no. 8105807.
[7] J. Wang, K. Atallah, and W. Wang, "Analysis of a magnetic screw for high force density linear electromagnetic actuators," *IEEE Trans. Magn.*, vol. 47, no. 10, pp. 4477–4480, Oct. 2011.
[8] U. Deshpande, "Two-dimensional finite-element analysis of a high-force-density linear switched reluctance machine including three-dimensional effects," *IEEE Trans. Ind. Appl.*, vol. 36, no. 4, pp. 1047–1052, Jul. 2000.
[9] T. J. Woolmer and M. D. McCulloch, "Analysis of the yokeless and segmented armature machine," in *Proc. IEEE Int. Electr. Mach. Drives Conf.*, vol. 1. May 2007, pp. 704–708.
[10] B. Zhang, T. Seidler, R. Dierken, and M. Doppelbauer, "Development of a yokeless and segmented armature axial flux machine," *IEEE Trans. Ind. Electron.*, vol. 63, no. 4, pp. 2062–2071, Apr. 2016.
[11] J. Wang and W. Wang, "A yokeless linear permanent magnet machine," *IEEE Trans. Magn.*, vol. 50, no. 11, Nov. 2014, Art. no. 81026040.
[12] A. Gandhi and L. Parsa, "Thrust optimization of a flux-switching linear synchronous machine with yokeless translator," *IEEE Trans. Magn.*, vol. 49, no. 4, pp. 1436–1443, Apr. 2013.
[13] R. W. Cao, Z. Zhang, and Y. Jin, "Double-sided linear flux-switching permanent magnet motor with yokeless secondary and control system," *Proc. CSEE*, vol. 37, no. 22, pp. 6585–6593, Nov. 2017.
[14] Y. Shen, Q. Lu, H. Li, J. Cai, X. Huang, and Y. Fang, "Analysis of a novel double-sided yokeless multitooth linear switched-flux PM motor," *IEEE Trans. Ind. Electron.*, vol. 65, no. 2, pp. 1837–1845, Feb. 2018.
[15] D. L. Trumper, W.-J. Kim, and M. E. Williams, "Design and analysis framework for linear permanent-magnet machines," *IEEE Trans. Ind. Appl.*, vol. 32, no. 2, pp. 371–379, Mar. 1996.
[16] J. Wang, G. W. Jewell, and D. Howe, "A general framework for the analysis and design of tubular linear permanent magnet machines," *IEEE Trans. Magn.*, vol. 35, no. 3, pp. 1986–2000, May 1999.
[17] J. Wang and D. Howe, "Tubular modular permanent-magnet machines equipped with quasi-Halbach magnetized magnets-part I: Magnetic field distribution, EMF, and thrust force," *IEEE Trans. Magn.*, vol. 41, no. 9, pp. 2470–2478, Sep. 2005.
[18] I. I. Abdalla, T. Ibrahim, and N. M. Nor, "Analysis of tubular linear motors for different shapes of magnets," *IEEE Access*, vol. 6, pp. 10297–10310, 2018.
[19] K. J. Meessen, B. L. J. Gysen, J. J. H. Paulides, and E. A. Lomonova, "Halbach permanent magnet shape selection for slotless tubular actuators," *IEEE Trans. Magn.*, vol. 44, no. 11, pp. 4305–4308, Nov. 2008.

QIAN WANG (M'09) received the Ph.D. degree in electrical engineering from the Harbin Institute of Technology, Harbin, China, in 2011.

Since 2011, he has been with the Institute of Specials Motors and Control, Harbin Institute of Technology. He is currently an Associate Professor with the Harbin Institute of Technology. His research interests include novel permanent magnet machines and drives, linear machines, and special electromagnetic actuation systems.

YINGQI CHEN received the bachelor's degree in electrical engineering from the Harbin Institute of Technology, in 2018, where he is currently pursuing the master's degree in electrical engineering.

His research interest includes permanent magnet machines and drives.

YAN GUO received the master's degree in electrical engineering from the Harbin Institute of Technology, in July 2019.

He is currently with Huawei Technologies Company Ltd. His research interest includes novel permanent magnet machines for EV applications.

JUAN ZHANG received the master's degree in electrical engineering from the Harbin Institute of Technology, in 2010.

She is currently with the Industrial Technology Research Institute of Heilongjiang Province, China.

YONG LI received the Ph.D. degree in electrical engineering from the Harbin Institute of Technology, in 1988.

He is currently a Professor with the Department of Electrical Engineering, Harbin Institute of Technology. His research interests include PMSMs, special motors, and their applications.

● ● ●